SOLAR CELLS

Efficient tandem solar cells with solution-processed perovskite on textured crystalline silicon

Yi Hou[1]*, Erkan Aydin[2]*, Michele De Bastiani[2]*, Chuanxiao Xiao[3]*, Furkan H. Isikgor[2], Ding-Jiang Xue[1], Bin Chen[1], Hao Chen[1], Behzad Bahrami[4], Ashraful H. Chowdhury[4], Andrew Johnston[1], Se-Woong Baek[1], Ziru Huang[1], Mingyang Wei[1], Yitong Dong[1], Joel Troughton[2], Rawan Jalmood[2], Alessandro J. Mirabelli[2], Thomas G. Allen[2], Emmanuel Van Kerschaver[2], Makhsud I. Saidaminov[1], Derya Baran[2], Qiquan Qiao[4], Kai Zhu[3], Stefaan De Wolf[2]†, Edward H. Sargent[1]†

Stacking solar cells with decreasing band gaps to form tandems presents the possibility of overcoming the single-junction Shockley-Queisser limit in photovoltaics. The rapid development of solution-processed perovskites has brought perovskite single-junction efficiencies >20%. However, this process has yet to enable monolithic integration with industry-relevant textured crystalline silicon solar cells. We report tandems that combine solution-processed micrometer-thick perovskite top cells with fully textured silicon heterojunction bottom cells. To overcome the charge-collection challenges in micrometer-thick perovskites, we enhanced threefold the depletion width at the bases of silicon pyramids. Moreover, by anchoring a self-limiting passivant (1-butanethiol) on the perovskite surfaces, we enhanced the diffusion length and further suppressed phase segregation. These combined enhancements enabled an independently certified power conversion efficiency of 25.7% for perovskite-silicon tandem solar cells. These devices exhibited negligible performance loss after a 400-hour thermal stability test at 85°C and also after 400 hours under maximum power point tracking at 40°C.

T hrough an intensive worldwide effort, perovskite solar cell (PSC) power conversion efficiencies (PCEs) have increased from an initial 3.8% to a certified 25.2% during the past decade (1, 2). This progress is based on the combination of materials properties such as a low energy required for crystal formation (3), a sharp optical absorption edge (4), and a tunable band gap (5) ideally suited for photovoltaic (PV) applications. The rapid development of PSCs is further enabled through the use of solution-based coating methods to deposit the semiconductors (6).

These properties also make PSCs attractive as top cells for tandem applications that use lower band gap bottom cells such as crystalline silicon (c-Si) and copper indium gallium selenide (CIGS) (7–18). By reducing thermalization losses, stacking PV absorbers of decreasing band gap in a multijunction device can overcome the Shockley-Queisser efficiency limit of 33.7% for single-junction solar cells. The combination with a c-Si bottom cell is of particular appeal, because single-junction c-Si–based technology has come to dominate the PV market. However, as c-Si solar cell efficiencies approach their practical limits, multijunction technologies using a c-Si bottom cell are of interest to drive further efficiency improvements.

Silicon heterojunction technology is attractive for tandem solar cells because of its high PCE and comparatively straightforward tandem integration. At present, most reported monolithic perovskite-silicon tandem devices are based on a single-side texturing configuration: c-Si wafers with their front flat-polished so that it is compatible with existing solution-based perovskite fabrication processes and a textured back side for enhanced light trapping relative to that of a double-side polished c-Si device (8, 14–16, 18). This configuration, however, provides limited light-trapping benefits and requires additional antireflection foils that do not provide sufficient light trapping compared with the textured counterpart (18). Furthermore, the effectiveness of antireflection foils can be compromised upon encapsulation. The preparation of such atomically smooth surfaces is also not practiced industrially owing to the high processing costs involved. Building up efficient tandems using double-side textured wafers—the industry-compatible c-Si approach—still challenges the PV community.

As a result, recent attention has shifted to combining perovskites with fully textured c-Si (7). The benefits of fully textured tandems have been demonstrated previously by Sahli et al. using a hybrid two-step deposition method combining sequential coevaporation of PbI$_2$ and CsBr and solution conversion (7). Unfortunately, the fill factor (FF) was moderate, a result of the limited perovskite quality achieved using this approach (19, 20). More efficient, but also more complex, thermal coevaporation enables textured tandems; however, the large vapor-pressure difference between the organic and inorganic components demands a high level of control over the deposition rates

of each precursor during the evaporation process (21).

Early efforts to deposit perovskites by using solution techniques on top of micrometer-sized Si pyramids quickly revealed a number of hurdles: uncovered Si pyramids, shunt paths, and inefficient charge collection in films with variable thickness. In addition, the application of conventional surface-passivation techniques—a prerequisite for state-of-the-art PSC device performance—are incompatible with the rough perovskite surfaces that result from the underlying c-Si texture (7). So far, insulating solution-processed passivants have failed to cover rough surfaces with the needed consistency of a thickness of a few nanometers.

Previous reports of perovskite-silicon tandems atop textured c-Si bottom cells have relied on physical vapor deposition of the perovskite front cell, rather than solution-processed perovskite cells on textured c-Si bottom cells. We sought to develop a high-quality micrometer-thick perovskite to cover the pyramids and, simultaneously, to enhance charge collection in these thick films through improved drift and diffusion of photogenerated carriers. We combined solution-processed, micrometer-thick, wide–band gap perovskite solar cells with pyramidal-textured c-Si bottom cells. This approach achieved a threefold enhanced depletion width in the perovskite semiconductor at the valleys of Si pyramids, improving carrier collection, as revealed using nanometer-scale kelvin probe force microscopy (KPFM).

To further increase carrier diffusion length, we introduced a conformal surface-passivation strategy for rough surfaces by anchoring a self-limiting passivant on the wide–band gap perovskite surface. This passivant also suppresses phase segregation. In addition, micrometer-thick perovskites allowed us to maintain a plateau of external quantum efficiency (EQE) of 92 to 93% across the spectral range of 650 to 730 nm. The fully textured bottom cells minimized reflection losses and efficient light trapping was achieved for the bottom cells, crucial to satisfying current-matching conditions. Overall, with the combined enhancements in charge drift and diffusion, the best tandem cells herein achieved an independently certified efficiency of 25.7%, combined with negligible performance loss after 400-hour thermal-stability tests at 85°C and also after 400 hours under maximum power point (MPP) tracking at 40°C.

As seen in the scanning electron microscope (SEM) top-view images, the textured c-Si features 2-μm-sized (111) faceted pyramids that were fabricated by alkaline wet-chemical etching (Fig. 1A). When forming tandems atop a textured c-Si bottom cell, it is important that one control the perovskite morphology and film thickness. When the perovskite film was deposited under fabrication conditions used for conventional planar perovskites (generally
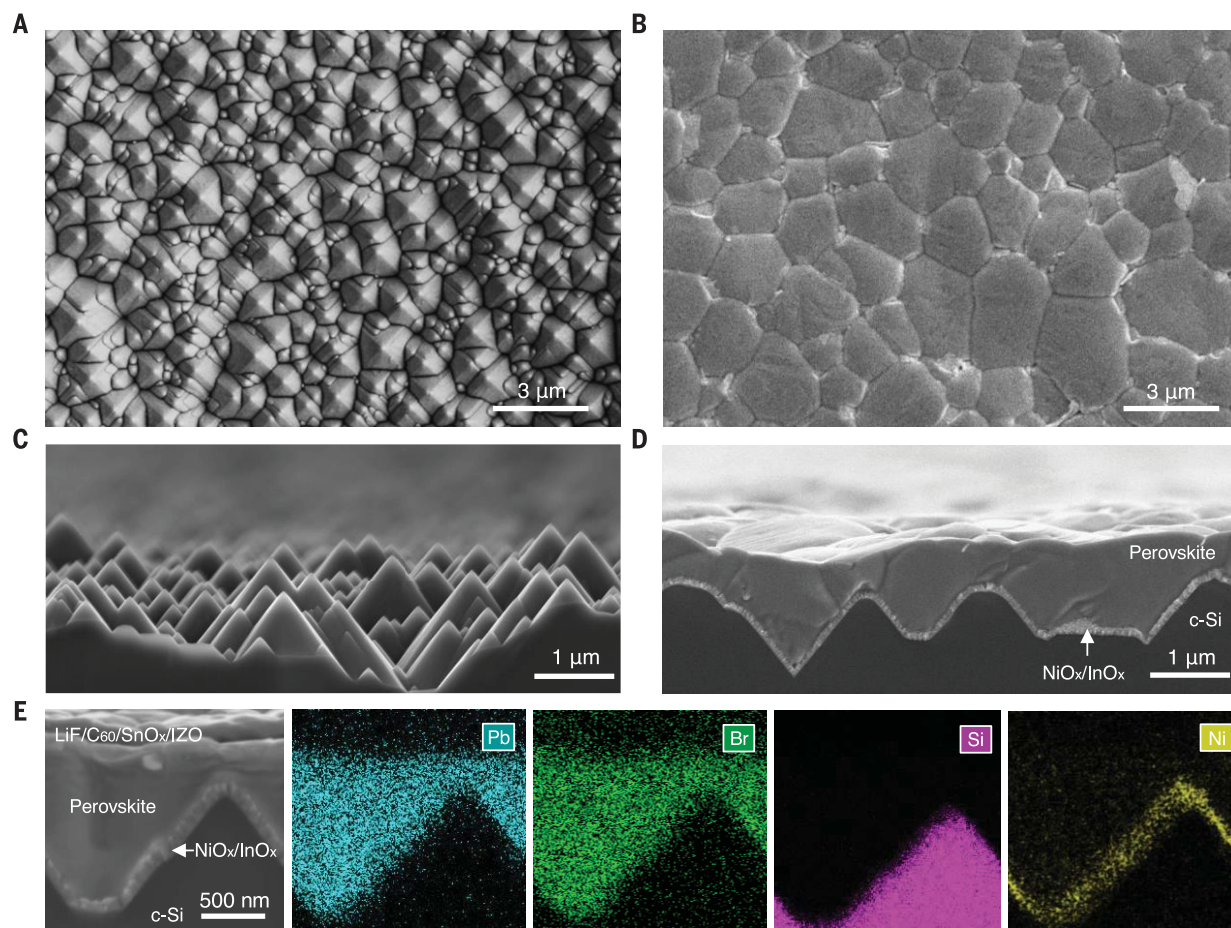
Fig. 1. Microstructure of solution-processed perovskite top cells on textured c-Si bottom cells. (**A** and **B**) SEM top-view images of the textured c-Si surface with an average pyramid size of 2 μm (A) and corresponding substrates covered by solution-processed perovskite crystal (B). (**C** and **D**) SEM cross-section images of a textured c-Si with an average pyramid size of 2 μm (C) and corresponding substrates covered by solution-processed perovskite crystal (D). (**E**) SEM image with corresponding EDS maps indicating the distribution of lead (Pb, aqua), bromide (Br, green), silicon (Si, purple), and nickel (Ni, yellow) inside the solar cell. Lead and bromide distribution were confined to the perovskite layer.

resulting in 400- to 600-nm-thick films), pyramids that were not capped with perovskite were observed, and these regions created shunt paths in devices (fig. S1). To fully cover the micrometer-sized pyramids, we used a concentrated (1.65 to 1.75 M) precursor that resulted in a micrometer-thick perovskite with large (2 to 4 μm) grain sizes (Fig. 1B). This process enabled us to achieve uniform perovskite coverage of the pyramids and eliminated the need for additional flattening processes (Fig. 1, C and D).

To achieve current matching, we opted to broaden the band gap of the micrometer-thick perovskite rather than reduce the thickness of a smaller–band gap perovskite because the latter approach would uncover pyramids. This thick, wide–band gap perovskite (1.68 eV, $Cs_{0.05}MA_{0.15}FA_{0.8}PbI_{2.25}Br_{0.75}$) top cell also provided a path toward a higher ultimate efficiency limit in tandem solar cells (fig. S2).

Because the size of the Si pyramids and perovskite thickness were similar, this infiltrated morphology differs from previously reported flat and conformal architectures used in perovskite-silicon tandem devices (fig. S3) (7, 8, 14, 15). These images also suggest that the textured structures substantially modified the surface geometry by increasing the contact area. Rather than producing a conformal coating with uniform thickness, which would be similar to the evaporation case, the solution-processed perovskite smoothly overcoated the pyramid geometry while retaining the curvature of the textured surface beneath (Fig. 1D). The elemental distribution within the tandems measured by means of energy-dispersive x-ray spectroscopy (EDS; Fig. 1E) confirmed the presence of a textured layer stack. From the detailed features of the perovskite and conformal NiO_x interface, we did not see undesired accumulation of hole-transport layer (HTL) material at the bottom, nor did we observe HTL material absence at the facets of the Si pyramids (7, 8, 14, 15).

Thick perovskite layers require sufficiently long charge-carrier diffusion lengths to enable efficient charge collection. This condition demands perovskite crystals and surfaces of high electronic quality. To increase the performance of single-junction wide–band gap PSCs, much research has focused on developing surface treatments (22). Trioctylphosphine oxide (TOPO) can substantially reduce nonradiative recombination and increase perovskite stability (23), but its insulating nature inhibits charge transport in devices. In addition, the rough surface of textured c-Si devices sets an additional challenge in the search for surface passivation. A passivant film must conformally coat and passivate the rough top perovskite surface with readily controlled thickness and functional groups without being overly sensitive to surface topography, treatment time, and perovskite thickness. Moreover, this treatment should not dissolve the perovskite nor alter its crystal structure (24).

We pursued an approach in which we exposed the rough perovskite top surface to 1-butanethiol vapor, a technique adapted in light of previous work performed on thiol-based self-assembled monolayer growth on metal surfaces. The thiol group anchored to the perovskite surface by strong coordination of the thiol on Pb^{2+}. The thiol molecules rapidly
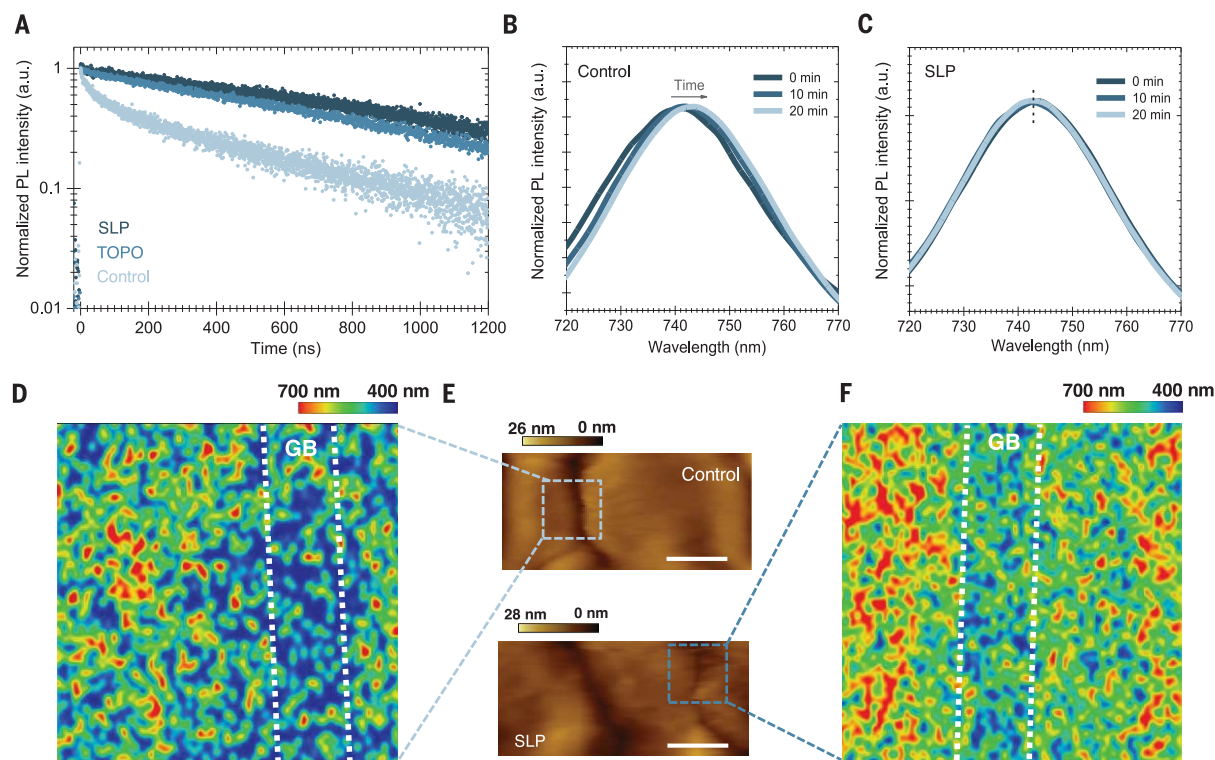
Fig. 2. Effects of SLP on diffusion length and phase segregation in micrometer-thick wide–band gap perovskite. (**A**) TRPL spectra of 1.68-eV–band gap thin films under different surface treatments. a.u., arbitrary units. (**B**) Normalized PL spectra of control perovskite films after illuminating for 0, 10, and 20 min. (**C**) Normalized PL spectra of SLP-treated perovskite films after illuminating for 0, 10, and 20 min. (**D**) Nanoscale-resolved mapping of the area indicated by the light blue square in (E) (100 nm by 100 nm) of the diffusion length of the control perovskite. The white dashed line shows the corresponding grain-boundary (GB) area. (**E**) Contact-mode atomic force microscopy (AFM) topography of the control sample (top) and SLP perovskite (bottom) (scale bar, 100 nm). (**F**) Nanoscale-resolved mapping of the area indicated by the dark blue square in (E) (100 nm by 100 nm) of the diffusion length of the SLP perovskite. The white dashed line shows the corresponding GB area.

diffused through the vapor phase to the perovskite surface, in contrast with thiol passivation of PbS colloidal quantum dots, where ligand exchange occurred in solution. Because of the self-limiting nature of thiol passivation, no anchoring sites were present after the initial passivation for further growth of additional layers. Thus, prolonged exposure did not damage the perovskite.

We used ultrafast transient absorption spectroscopy to investigate the phase distribution of 1.68-eV–band gap perovskite films after different treatment times. The two classes of treated films each showed a single ground-state bleaching peak centered at ~725 nm (fig. S4). This result indicated that the perovskite films existed compositionally within a single phase and that the bulk properties of the perovskite film could be stabilized with the thiol self-limiting passivation (SLP) treatment. We confirmed identical recombination kinetics for the film after 30-min and 20-hour SLP treatments: The data (fig. S4) attest to the time-insensitivity of the passivation process. Similarly, there were no differences in surface-sensitive grazing-incidence wide-angle x-ray scattering (GIWAXS) measurements between

the samples with different SLP treatment times. After different treatment times, the perovskite peaks maintained their intensities and positions, suggesting no change in crystal structure and orientation (fig. S5).

After SLP treatment, we observed in time-resolved photoluminescence (TRPL) an increase in the carrier lifetime from 570 to 900 ns when we measured the samples from air-perovskite sides. This is ~15% higher than that of similar films treated with TOPO (Fig. 2A) and ~60% higher than that of control samples. We propose that passivation using smaller-sized thiols provided increased diffusion through the vapor phase and reduced steric hindrance. When we illuminated from the glass-perovskite side, the carrier lifetime was essentially similar in these three samples (fig. S6). Passivation was most effective on the top surface of thick perovskite, where, in the pristine case, major carrier recombination would otherwise have occurred.

The SLP treatment also enhanced phase stability of the perovskite. After 20 min of continuous light exposure, the SLP-treated films exhibited a stable PL peak position, whereas the control sample showed a red shift in the peak position, indicative of phase segregation

(Fig. 2, B and C). This result is in agreement with earlier conclusions from Belisle *et al.* demonstrating that charge accumulation and carrier trapping at perovskite surfaces are drivers of photoinduced halide segregation and that efficiently passivating the perovskite surfaces suppresses phase segregation and stabilizes wide–band gap perovskites (*25*).

A representative, randomly selected 100-nm–by–100-nm area for topographic imaging that included grain boundaries (red square in fig. S7) was mapped for the nanoscale charge-carrier diffusion length, which is related to the local charge-carrier transport time (fig. S8) and charge-carrier recombination lifetime (fig. S9). Figure 2, D to F, presents nanoscale diffusion-length maps of both control sample and SLP-treated perovskite at similar regions, indicated by the blue squares. The diffusion length was improved in both grain and grain boundaries for SLP perovskites compared with control samples. The diffusion length in SLP perovskites within grains was ~570 nm. At the grain boundaries, the diffusion length of the SLP perovskite decreased by ~50 nm, whereas the diffusion length in the control sample decreased by ~100 nm (fig. S10). Thus,
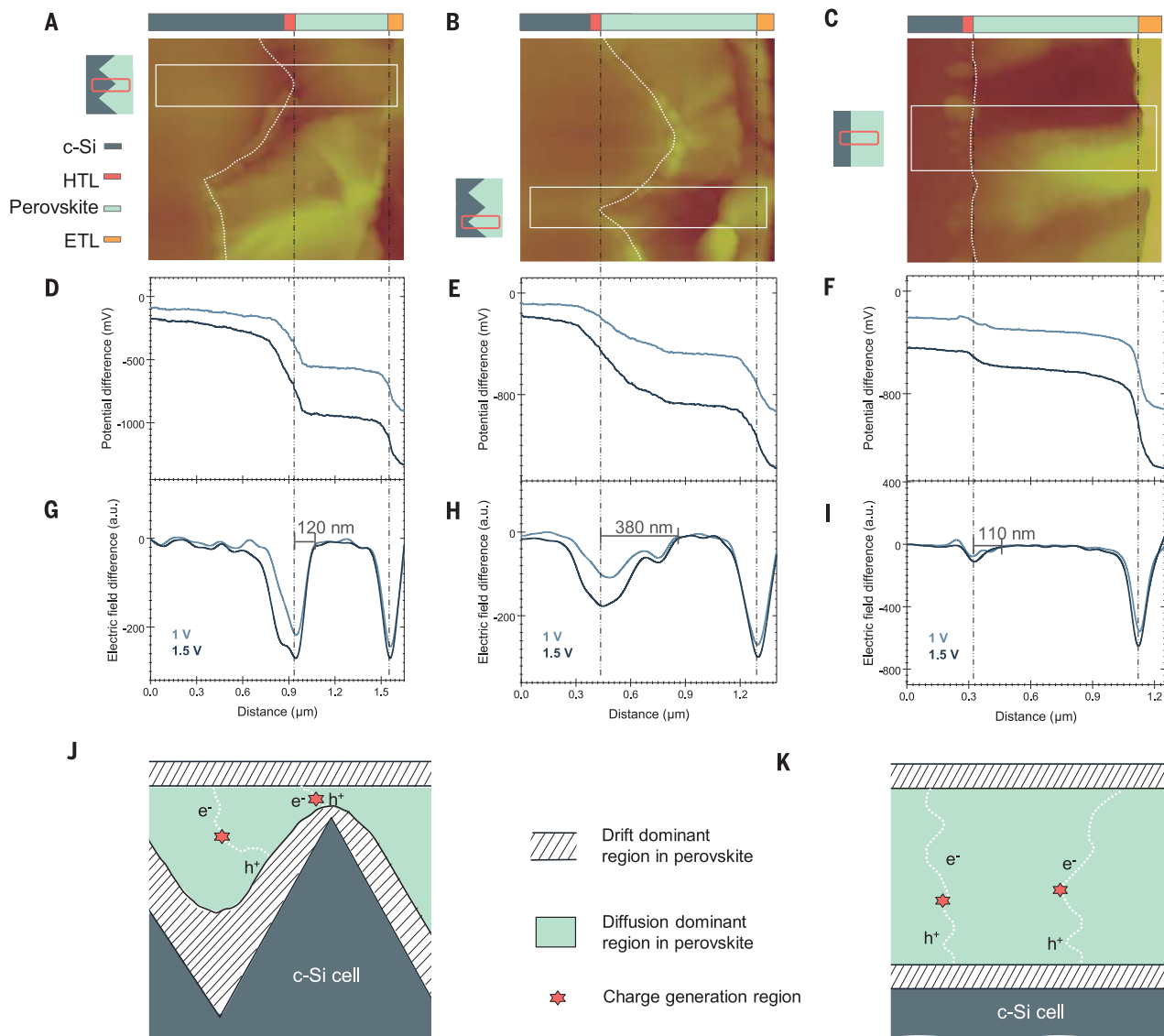
Fig. 3. Enhanced charge extraction in textured structured tandem cells.
(**A** to **C**) AFM image of a cross section of the peak of a pyramid in the textured and flat tandem with a schematic showing each layer across the top of the Si bottom cell and the corresponding measured electric-potential zone. (**D** to **F**) Potential-difference profiling across the device under different bias voltages subtracted from the 0 V curve. (**G** to **I**) Electric-field difference across the device, taken by the first derivative in (D) to (F). (**J** and **K**) Schematics of electric-field distribution in textured (J) and flat tandem devices (K). h^+, holes; e^-, electrons.

passivation of the grain boundaries for the SLP perovskite increased the charge diffusion length compared with the control sample.

To probe the effects of the textured structure on the electrical field in the vertical direction, we used nanometer-scale KPFM to profile and observe the differences in electric-potential (or electric-field) distribution across the flat and textured devices. To determine the bulk profile from the surface measurement, we applied different forward-bias voltages of 1 and 1.5 V to the device and imaged the cross-sectional surface potential under each voltage (figs. S11 to S20). The junction characteristic was assessed from the small current flow, or

equivalent shunt resistance, under bias, which was acquired by measuring the voltage drop across the cross-sectional surface.

By taking the first derivative of the potential difference, we determined the electric-field distribution relative to the metallurgical interfaces (Fig. 3, A to I). We observed two prominent junction peaks at the HTL-perovskite and perovskite–electron-transport layer (ETL) interfaces, whereas the electric field was near zero inside the perovskite layer. The perovskite-ETL junction has a similar strength and depletion width for both flat and textured cells, which agreed with the perovskite-ETL interfaces being identical for these two

devices. Interestingly, the electric field at the HTL-perovskite interface was enhanced when a textured substrate was used (Fig. 3, J and K).

We determined that the depletion region in the perovskite (at the HTL-perovskite interface) was much wider at the valley of Si pyramids (~380 nm) than at their top (~120 nm) or compared with flat perovskite cells. This result implies that where the perovskite was the thickest, the depletion width was the largest, which would be desirable for effective charge collection. At the pyramid valleys, the perovskite was more confined and was subjected to electrical fields superimposed from neighboring HTL-coated pyramids. When Si
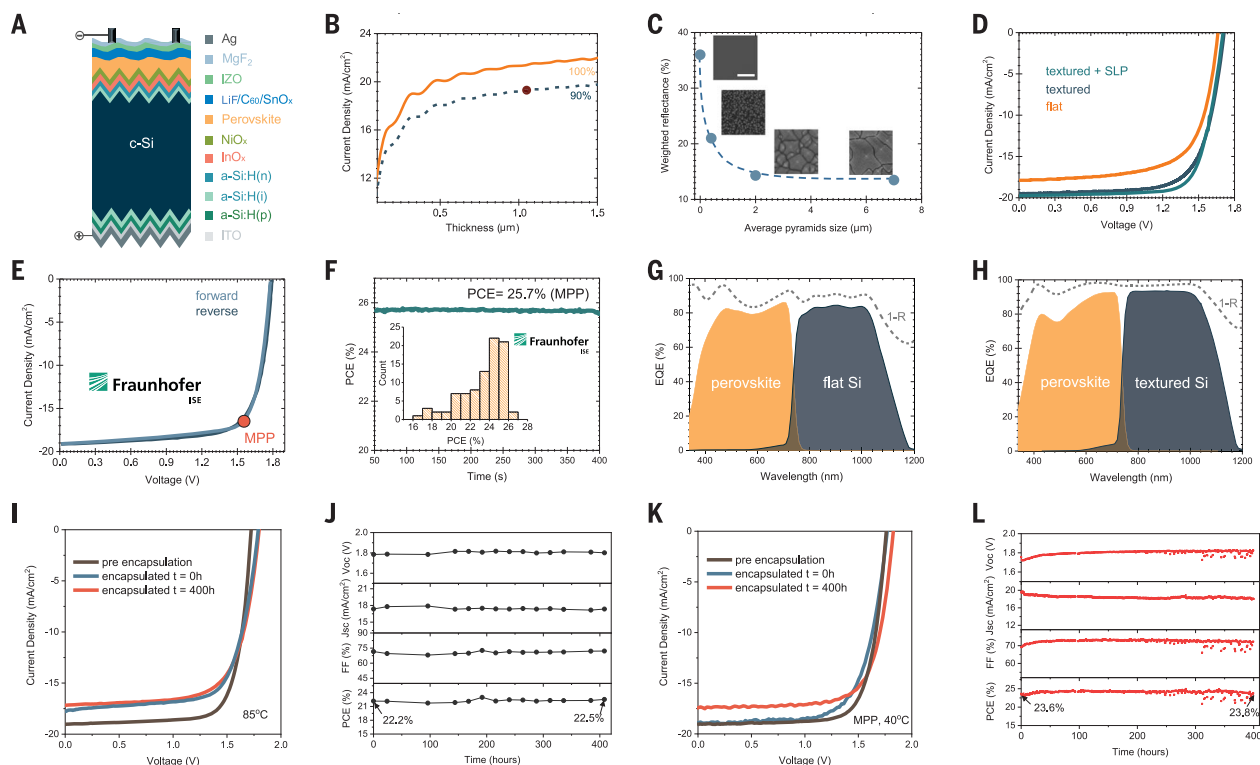
Fig. 4. Device characterization and stability of tandems. (**A**) Schematic of solution-processed perovskite–textured silicon tandem architecture. a-Si:H(n), n-doped hydrogenated amorphous silicon; a-Si:H(i), intrinsic hydrogenated amorphous silicon; a-Si:H(p), p-doped hydrogenated amorphous silicon. (**B**) Calculated J_{SC} values of the perovskite cells as a function of perovskite layer thickness. The red dot represents the EQE-integrated J_{SC} value in the textured tandem top cell. (**C**) Measured weighted reflectance as a function of pyramid sizes of c-Si. Texturing size refers to the pyramid base. The SEM images of different texturing sizes are reported in the insets (scale bar, 2 μm). (**D**) J-V characteristics of flat, textured, and SLP-treated textured tandems. (**E**) J-V characteristics of certified SLP-treated textured tandems. (**F**) MPP tracking of certified SLP-treated textured tandems and PCE distributions of 88 individual tandem devices. (**G** and **H**) EQE of the flat (G) and textured (H) devices (integrated current of 18.2 mA/cm² for the top cell and 16.8 mA/cm² for the bottom cell in the flat device; 19.3 mA/cm² for the top cell and 19.2 mA/cm² for the bottom cell in the Fraunhofer ISE CalLab PV Cells–certified textured device). (**I**) J-V curves of tandem devices before encapsulation (glass and butyl rubber) at the beginning and the end of the 85°C stability test. (**J**) J-V parameters measured over a 400-hour stability test at 85°C (relative humidity ~45 to 50%). (**K**) J-V curves of the tandem devices before encapsulation (glass and POE) at the beginning and the end of the MPP stability tests. (**L**) J-V parameters measured over >400 hours of light-soaking under MPP load at 40°C.

pyramid valleys were sharper, depletion regions were wider (in a linear relation; detailed values are shown in tables S1 and S2), which further suggested that the depletion width correlates with the geometry factor. In contrast with the case of other deposition methods (such as coevaporation), this geometry was only observed when the solution-processed perovskite cells smoothed out the textured silicon cell and caused this beneficial geometry-dependent electric-field distribution. This finding agrees with the simulated results (fig. S21).

The KPFM observation accounted for device performance trends, in that charge collection was enhanced in the best pyramid devices. The stronger and wider depletion at the valley of the pyramids benefited charge collection of charge carriers photogenerated with long-wavelength incident light. Outside of the depletion region, the carriers needed to diffuse through the perovskite absorber layer to be collected. At the top of the Si pyramids, the depletion width was not broadened. However, here the distance between hole contact and

electron contact was much shorter (100 to 300 nm), which was well within the typical range of efficient charge diffusion in a PSC (Fig. 3, J and K). In light of the surrounding pyramidal structure, charges generated in the textured perovskite had a shortened transport distance to both contacts compared with a flat perovskite cell.

Figure 4A sketches the cross section of the textured tandem. To explore the role of the thick perovskite, we studied the thickness-dependent current generation theoretically. As presented in Fig. 4B, the short-circuit current density (J_{SC}) of the perovskite cell increased with layer thickness. The red dot represents the experimental J_{SC} value of the ~1.1-μm-thick perovskite used in this work (fig. S22), which is within <10% of the theoretical limit. This certified ~19.3 mA/cm² value is among the highest values for a single-pass device with 1.68-eV–band gap perovskites (Fig. 4H). In contrast with opaque devices with reflection from the rear electrode, single-junction devices required a thicker absorber to capture

more photons near the band edge. With more photons absorbed by the top cell, we expect an enhanced upper limit of tandem efficiency.

Spectrally weighted reflectances were calculated from the air mass (AM) 1.5 G spectrum in the range of 350 to 900 nm (Fig. 4C). To investigate the effect of pyramid size on the reflection loss, we also selected different Si pyramid sizes by tailoring the texturing process. Although the pyramids in commercial Si are typically in the range of 2 to 7 μm, the benefit to reflection began to saturate when the pyramid size reached 2 μm or less (see fig. S23). This result is encouraging for perovskite-silicon tandems because it suggests that well-established solution-processing techniques can be united with textured silicon (fig. S24).

We observed enhanced J_{SC} and FF in tandems (Fig. 4D and figs. S24 and S25) in the case of fully textured c-Si bottom cells. EQE measurements highlight the advantage of switching from a polished front side to a double-side textured architecture (Fig. 4, G and H). Reflections occurring in the flat design

induced more current loss in the 330- to 1200-nm range. The introduction of a front texture reduced the overall reflectance, especially at wavelengths of 550 and 800 nm. The J_{SC} integrated from the EQE spectra is in excellent agreement with that derived from the 1-sun current density–voltage (J-V) curve with enhanced J_{SC} in both the top cell and bottom cell on the double-side textured device.

Both differential EQE and absorption confirm the ~1.68-eV perovskite band gap (fig. S2). We observed narrower EQE overlap between the perovskite and Si cell. The textured-device EQE maintained a plateau at 92 to 93% in this region. This result is distinct from previous work based on 400- to 600-nm-thick perovskite on flat devices in which the perovskite lost EQE at wavelengths of 550 and 800 nm. This high EQE photocurrent, combined with enhanced charge extraction, resulted in high FF, leading to an improved device performance from 20.3 to 24.0% (table S3). In particular, by further adding SLP treatment, we observed a distinct increase of FF from 72 to 77% (Fig. 4D). By reducing the recombination area and improving the top contact design (fig. S26), we achieved a Fraunhofer ISE CalLab PV Cells–certified stabilized (at MPP) PCE of 25.7% (Fig. 4, E and F, and fig. S27).

The tandems reported herein show low hysteresis (Fig. 4E), high reproducibility (Fig. 4F and fig. S28), and excellent operational stability under accelerated tests (Fig. 4, I to L). We monitored the stability of devices encapsulated with glass and butyl rubber. We heated these devices to 85°C for 400 hours in the dark at ~40% relative humidity and found that the devices retained their original performance (Fig. 4, I and J). We also monitored 400-hour operating stability of devices encapsulated using glass and POE (polyolefin encapsulant): Here, we used 1-sun-equivalent illumination (fig. S29) at 40°C and ~40 to 50% relative humidity (Fig. 4, K and L). J-V curves in both scan directions [open-circuit voltage (V_{OC}) to J_{SC} and J_{SC} to V_{OC}] were measured at 10-min intervals at 100 mV/s from −0.1 to +1.9 V, and vice versa. Between measurements, the tandem solar cell was held at the MPP voltage as determined by the most recent J-V scan. Devices retained their original performance after 400 hours. In Fig. 4, I to K, the J-V curves of the tandem were reported before encapsulation, at the beginning of the test, and after 400 hours, and images are provided of devices at the end of the test. Overall, we attribute this good operating lifetime to the replacement of organic carrier-selective layers with NiO_x inorganic materials, which prevent iodine reaction with small-molecule organic HTLs (table S4).

REFERENCES AND NOTES

1. A. Kojima, K. Teshima, Y. Shirai, T. Miyasaka, J. Am. Chem. Soc. 131, 6050–6051 (2009).
2. National Renewable Energy Laboratory, Best research-cell efficiencies (2020); www.nrel.gov/pv/cell-efficiency.html.
3. J. S. Manser, M. I. Saidaminov, J. A. Christians, O. M. Bakr, P. V. Kamat, Acc. Chem. Res. 49, 330–338 (2016).
4. S. De Wolf et al., J. Phys. Chem. Lett. 5, 1035–1039 (2014).
5. D. P. McMeekin et al., Science 351, 151–155 (2016).
6. Y. Deng et al., Nat. Energy 3, 560–566 (2018).
7. F. Sahli et al., Nat. Mater. 17, 820–826 (2018).
8. M. Jošt et al., Energy Environ. Sci. 11, 3511–3523 (2018).
9. Q. Han et al., Science 361, 904–908 (2018).
10. S. Essig et al., Nat. Energy 2, 17144 (2017).
11. M. Saliba et al., Science 354, 206–209 (2016).
12. G. E. Eperon et al., Science 354, 861–865 (2016).
13. J. Tong et al., Science 364, 475–479 (2019).
14. B. Chen et al., Joule 3, 177–190 (2019).
15. K. A. Bush et al., Nat. Energy 2, 17009 (2017).
16. H. Shen et al., Sci. Adv. 4, eaau9711 (2018).
17. F. Fu et al., Nat. Energy 2, 16190 (2016).
18. J. Zheng et al., Energy Environ. Sci. 11, 2432–2443 (2018).
19. W. S. Yang et al., Science 356, 1376–1379 (2017).
20. Q. Jiang et al., Nat. Photonics 13, 460–466 (2019).
21. L. Gil-Escrig et al., Adv. Energy Mater. 8, 1703506 (2018).
22. E. Aydin, M. De Bastiani, S. De Wolf, Adv. Mater. 31, e1900428 (2019).
23. I. L. Braly et al., Nat. Photonics 12, 355–361 (2018).
24. D. W. deQuilettes et al., Science 348, 683–686 (2015).
25. R. A. Belisle et al., ACS Energy Lett. 3, 2694–2700 (2018).

SUPPLEMENTARY MATERIALS

science.sciencemag.org/content/367/6482/1135/suppl/DC1
Materials and Methods
Figs. S1 to S29
Tables S1 to S4
References (26–31)

Science

Efficient tandem solar cells with solution-processed perovskite on textured crystalline silicon

Yi Hou, Erkan Aydin, Michele De Bastiani, Chuanxiao Xiao, Furkan H. Isikgor, Ding-Jiang Xue, Bin Chen, Hao Chen, Behzad Bahrami, Ashraful H. Chowdhury, Andrew Johnston, Se-Woong Baek, Ziru Huang, Mingyang Wei, Yitong Dong, Joel Troughton, Rawan Jalmood, Alessandro J. Mirabelli, Thomas G. Allen, Emmanuel Van Kerschaver, Makhsud I. Saidaminov, Derya Baran, Qiquan Qiao, Kai Zhu, Stefaan De Wolf and Edward H. Sargent

Growing perovskite on textured silicon

Wide–band gap perovskites could boost the efficiency of silicon solar cells by forming tandem cells, but usually the perovskite must be grown on a smoothed side of the silicon cell because the material grown on the rough light-trapping side often does not fully coat the silicon surface and its rough texture is prone to phase separation. Hou *et al.* grew thick films of a perovskite with a band gap of ~1.68 electron volts and used a passivant, 1-butanethiol, to limit its phase separation. The tandem cells had a certified power conversion efficiency of 25.7% and had negligible losses after 400 hours of operation.

Science, this issue p. 1135

ARTICLE TOOLS	http://science.sciencemag.org/content/367/6482/1135
SUPPLEMENTARY MATERIALS	http://science.sciencemag.org/content/suppl/2020/03/04/367.6482.1135.DC1
REFERENCES	This article cites 30 articles, 8 of which you can access for free http://science.sciencemag.org/content/367/6482/1135#BIBL
PERMISSIONS	http://www.sciencemag.org/help/reprints-and-permissions

Use of this article is subject to the Terms of Service